Multiscale Evaporation Rate Measurement Using Microlaser-Induced Fluorescence

Youngjoon Suh
Department of Mechanical and Aerospace Engineering,
University of California, Irvine,
Irvine, CA 92697

Cheng-Hui Lin
Department of Mechanical and Aerospace Engineering,
University of California, Irvine,
Irvine, CA 92697

Hamsa Gowda
Department of Biomedical Engineering,
University of California, Irvine,
Irvine, CA 92697

Yoonjin Won
Department of Mechanical and Aerospace Engineering,
University of California, Irvine,
Irvine, CA 92697

As the heat generation at device footprint continuously increases in modern high-tech electronics, there is an urgent need to develop new cooling devices that balance the increasing power demands. To meet this need, cutting-edge cooling devices often utilize microscale structures that facilitate two-phase heat transfer. However, it has been difficult to understand how microstructures enhance evaporation performances through traditional experimental methods due to low spatial resolution. The previous methods can only provide coarse interpretations on how physical properties such as permeability, thermal conduction, and effective surface areas interact at the microscale to effectively dissipate heat. This motivates researchers to develop new methods to observe and analyze local evaporation phenomena at the microscale. Herein, we present techniques to characterize submicron to macroscale evaporative phenomena of microscale structures by using microlaser-induced fluorescence (μLIF). We corroborate the use of unsealed temperature-sensitive dyes by systematically investigating the effects of temperature, concentration, and liquid thickness on the fluorescence intensity. Considering these factors, we analyze the evaporative performances of microstructures using two approaches. The first approach characterizes the overall and local evaporation rates by measuring the solution drying time. The second approach employs an intensity-to-temperature calibration curve to convert temperature-sensitive fluorescence signals to surface temperatures, which calculates the submicron-level evaporation rates. Using these methods, we reveal that the local evaporation rate between microstructures is high but is balanced with a large capillary-feeding. This study will enable engineers to decompose the key thermofluidic parameters contributing to the evaporative performance of microscale structures. [DOI: 10.1115/1.4046767]

1 Introduction

Over the past several decades, modern electronics continuously exceed their performance limits and get smaller, stimulating needs to develop high-performance cooling devices that meet the increasing power density [1]. Among various cooling apparatus, two-phase cooling devices, such as vapor chambers [2], capillary pumped loop heat pipes [2,3], loop heat pipes [2–5], and thermosyphon heat pipes [6], have shown great potential as a remedy for thermal management issues. In general, these devices operate in an evaporation, liquid-transport, and condensation cycle that utilize micro/nanoscale structures called the wick (Fig. 1(*a*)) [2,7,8]. The wick plays a vital role within the cooling devices by vaporizing, absorbing, and transporting the working fluid to maximize heat dissipation. Therefore, an optimal wick should have properties such as efficient working-fluid delivery (i.e., permeability) [4,9], large surface area to volume ratios [10], low thermal resistance [6], and high effective thermal conductivity [6].

Many heat transfer experiments analyze the wick's heat transfer (i.e., evaporative) performance at the device scale [4,11–13], which makes designing optimal wicks an arduous, trial-and-error task. While conventional "low spatial resolution approaches" are useful for pragmatic assessment of the whole device, it is difficult to precisely predict and optimize the wick's evaporative performance, due to the interplaying thermophysical parameters such as permeability, thermal conductivity, and effective surface areas. Analyzing local microscale evaporative characteristics is thereby important to optimize wick structures for device level performance advances. Among various methods to characterize evaporation rates at such scales, a general method is to measure local surface temperature profiles and insert them into energy balance equations or diffusion mass balance equations [14–18].

Measuring small-scale thermal profiles becomes challenging, and numerous temperature measurement methods have emerged to address resolution limitations. For example, infrared (IR) thermography measures two-dimensional temperature profiles based on sample thermal emission [14,19–22]. However, IR imaging is limited to the scales above 3–5 μm due to the wavelength diffraction limit measured in the camera (>3 μm) [21,23]. Another popular method is thermochromic liquid crystal thermography, which uses temperature-sensitive colors reflected by crystals to measure temperatures with up to 0.1 K thermal resolution [15,21,24–26]. While thermochromic liquid crystal measurements support high resolution, the samples need additional treatment such as thin and uniform coatings to increase spatial resolution [21,26], which makes it unsuitable for observing unpaintable objects such as porous material [21]. Direct measurement employing scanning thermal microscopy (SThM) uses nanoscale probe apexes to map thermal profiles at high-resolutions (∼30 nm) [27–29]. However, the contact area of the probe to the sample can vary depending on the local sample geometry, which can lead to contact-related artifacts [30,31]. Finally, microthermocouple probes prove the most conventional among the measuring techniques; they are cheap and accurate, but too large to probe into submicron-level features without damaging the structure (i.e., smallest microthermocouple commercially available is 13–50 μm) [26].

As an emerging technique, laser-induced fluorescence (LIF) gains attention as a powerful tool to characterize thermal profiles at multiple scales with high fidelity. In general, LIF utilizes temperature-and light-sensitive molecules called fluorophores. At the macroscale, LIF has been conventionally used to analyze bulk thermofluidic physics typically over the mm scale [32–34]. On the other hand, microlaser-induced fluorescence (μLIF) employs fluorescent microscopes to improve spatial and thermal resolutions up

to 0.1–0.3 μm and 0.01 K, respectively [18,23,35–40]. The methods generally employ fluorescence, where temperature-sensitive fluorophores absorb photons of a specific wavelength (i.e., excitation) and emit photons of a longer wavelength (i.e., emission) (Fig. 1(b)). The emitted fluorescence signals are selectively transmitted through an optical filter to produce fluorescence intensity-based imaging, which is then converted into temperature-based pictures. A great advantage of using μLIF is to observe temporal micro/nanoscale pixel-based fluorescent intensity profiles of the liquid–vapor interface. In other words, even some of the smallest liquid–vapor surface features are easily detected by observing fluorescence signals and can be used to assess local drying phenomena in complex structures. Although μLIF techniques have shown potential to function as thermometers in closed systems [23,36,39], there are several inherent problems that could affect the measurement accuracy in an open system (where solvent is evaporating) such as photobleaching and thin-film evaporation. Photobleaching terminally alters the fluorophores and make them unable to fluoresce, but can be minimized by selecting photobleaching-resistant dyes and with careful control over the laser beam intensity [23,41]. On the other hand, the thin-film solvent evaporation effects on fluorescence behavior are not as simple to address because the liquid film thickness and dye concentration simultaneously change upon evaporation. Past studies report that fluorescence intensity increases with larger liquid thickness or with higher dye concentration [42,43]. However, the integrated effect of such two factors on fluorescence intensity remains unexplored.

Herein, we systematically present methods to characterize evaporative phenomena in an open system by using μLIF techniques at both large ($\sim$1 cm) and local (0.3–35 μm) scales. The proposed methods consider temperature, liquid thickness, and concentration effects on fluorescence intensity. For submicron level characterization, vapor transport equations are employed to calculate evaporation rates based on fluorescence intensity to temperature calibrations. Our results help decompose key physical parameters such as microscopic liquid flow paths that influence the wick's evaporative performance. Therefore, the insights of this study can promise technical advances toward applications requiring high-fidelity microscale thermophysical characterization.

2 Experimental Method

**2.1 Rhodamine B Solution.** We use laser grade rhodamine B (Acros Organics, Geel, Belgium) to make a temperature-sensitive fluorescent working fluid. Prior to rhodamine B addition, a 0.1 M sodium carbonate–bicarbonate buffer at pH 9.4 is prepared to ensure proper dye color density. The buffer is made by adding 30 ml of 0.1 M sodium carbonate to 70 mL of 0.1 M sodium bicarbonate. The buffer is then diluted from 0.1 M to 0.2 mM, and rhodamine B is added to make a 2 mM solution. The rhodamine B solutions are filtered with a syringe filter (0.2 μm pore size) before the use.

2.2 Evaporation Chip Fabrication. A custom-built evaporation chip is used for all experiments in this study. The evaporation chip consists of top and bottom acrylic platforms, a removable glass slide, a rubber gasket, spring-loaded pogo pins, and a transparent indium-tin-oxide (ITO) heater. The top and bottom platforms are fabricated using a computer numerical control router to provide rigid support for all components. The gasket is inserted between the glass slide and the top chip to prevent leakage by applying distributed pressure through bolts and nuts. A constant voltage is provided through a power supply to produce a constant heat flux of 0.75 Wcm^{-2} from the ITO heater to the glass slide.

2.3 Fabrication Process of Microscale Structures. The wicks are fabricated using a simple template-assisted electrodeposition method. A 1 mm thick brass plate is cut into 1 cm $\times$ 3 cm sample pieces through machining processes. A copper sample used as the anode is prepared with identical dimensions. The brass and copper samples are immersed in hydrochloric acid for 15 min prior to electrodeposition. The electrodeposition process is performed in a stationary 0.4 M CuSO$_4$ + 1.8 M H$_2$SO$_4$ solution. A constant current density of 2 Acm^{-2} is applied for 3 min with a power supply.

2.4 Image Acquisition. To obtain real-time, fluorescence-based liquid–vapor interface images, we use both inverted and upright confocal fluorescence microscopes.

The inverted microscope views objects from bottom to top and can greatly increase imaging precision by eliminating the need to continuously focus on dynamic liquid–vapor interfaces (Fig. S1(a) available in the Supplemental Materials on the ASME Digital Collection). Accordingly, we use an inverted microscope (LSM 700, ZEISS) with a 10 mm long working distance objective to characterize the liquid thickness and concentration effects on fluorescence intensity. An appropriate filter set (559 nm excitation
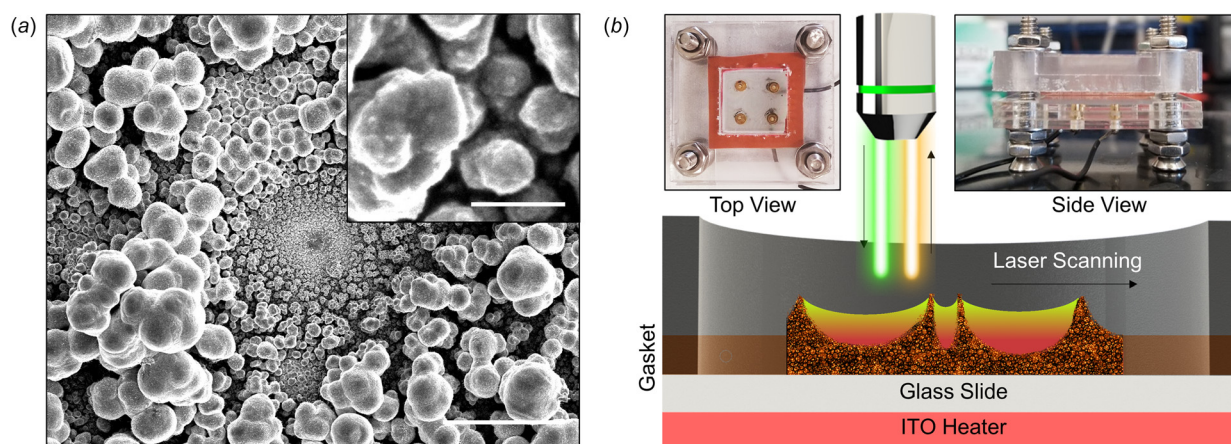
Fig. 1 Experimental setup to measure evaporative performance of microscale structures. (a) The porous structures used in this study show a highly interconnected network of coarse and fine copper particles as confirmed by scanning electron microscope image. The scalebar is 100 μm. The inset shows a magnified image of copper particles where the scalebar represents 2 μm. (b) The sample is mounted onto a glass slide where a heat flux of 0.75 Wcm^{-2} is applied by an ITO heater. A fluorescence dye solution is supplied through the porous copper structure and is excited by 559 nm wavelength laser. The emitted light passes through optical filters and is processed using a computer software to provide fluorescence imaging. The upper left and right insets show the top and side view of the chip, respectively.

bandpass and 570–800 nm emission bandpass) with a broadband halogen illumination is used.

On the other hand, the upright microscope enables surface imaging of opaque samples from top to bottom (Fig. S1(b) available in the Supplemental Materials on the ASME Digital Collection). Hence, an upright microscope (BX61, Olympus) is used to characterize evaporative performances of opaque microscale structures. A minimal laser beam intensity of 0.3% (to reduce photobleaching) excites the fluid at wavelengths of 559 nm to fluoresce while a fluorimeter records the fluorescence spectra. The high voltage and gain are set manually and are kept constant throughout a given set of experiments. Digital images are obtained and postprocessed with ZEN (ZEISS) and FLUOVIEW FV1000 (Olympus) software. Image colors are added through built-in channel options.

3 Mathematical Model

In Sec. 4.2.3, we calculate local evaporation rates based on surface temperatures by employing a species transport equation for vapor at the liquid–vapor interface [17,18]. By assuming that the equilibrium vapor pressure at the interface $p_{v\_equ}(T_{lv})$ is equivalent to the saturation pressure, the Clausius–Clapeyron equation provides an expression for the saturation pressure $p_{sat}(T_{lv})$

$$
\begin{aligned}
p_{v\_equ}(T_{lv}) &\approx p_{sat}(T_{lv}) \\
&= p_{sat\_ref}(T_{lv})\exp\left(\frac{Mh_{fg}}{R}\left(\frac{1}{T_{sat\_ref}} - \frac{1}{T_{lv}}\right)\right)
\end{aligned}
\tag{1}
$$

where $p_{sat\_ref}(T_{lv})$ is the reference saturation pressure of 1 atm, M is the vapor molecular weight, h_{fg} is the latent heat, T_{sat_ref} is the reference saturation temperature at 1 atm, R is the universal gas constant, and T_{lv} is the liquid–vapor temperature. On the other hand, the mass flux (i.e., evaporative mass flux $\dot{m}''$) at the liquid–vapor interface is provided through a general species transport equation

$$
\dot{m}''_v = M(-D\mathbf{n}\cdot\nabla C_v + u_n C_v)
\tag{2}
$$

where D is the diffusion coefficient, u is the fluid velocity, and C is the molar concentration. A similar equation can be written for air. Since there is no mass transport of air ($\dot{m}''_{air} = 0$) through the interface, the species transport equation for air becomes

$$
u_n|_{lv} = \frac{D}{C_{air}}(\mathbf{n}\cdot\nabla C_{air})|_{lv}
\tag{3}
$$

$$
u_n|_{lv} = -\frac{D}{C_{tot} - C_v}(\mathbf{n}\cdot\nabla C_v)|_{lv}
\tag{4}
$$

By substituting this to Eq. (2)

$$
\dot{m}''_v = -\frac{MD}{1 - C_v/C_{tot}}(\mathbf{n}\cdot\nabla C_v)|_{lv}
\tag{5}
$$

According to the ideal-gas law

$$
C_{tot}|_{lv} = \frac{p_{atm}}{RT_{lv}}
\tag{6}
$$

$$
C_v|_{lv} = \frac{p_{sat}(T_{lv})}{RT_{lv}}
\tag{7}
$$

Finally, ∇C_v is defined as

$$
\nabla C_v = \frac{C_v|_{lv} - C_v|_{far}}{L_{far}}
\tag{8}
$$

where $C_v|_{lv}$ is the molar concentration at the interface and $C_v|_{far}$ is the molar concentration at a distance $L_{far} = 3h$, and h is the

average structural thickness. Description of L_{far} is provided in Supplementary Information S2 available in the Supplemental Materials on the ASME Digital Collection.

4 Results and Discussion

4.1 Rhodamine B Characterization. In this section, we corroborate the feasibility of using unsealed rhodamine B to characterize evaporative phenomena by systematically investigating the effects of temperature, liquid thickness, and concentration on fluorescence intensity.

4.1.1 Temperature Effect on Fluorescence Intensity. We investigate the dye's temperature-sensitivity by recording its fluorescence intensity as a function of temperature by using a heated microchip (Fig. S3 available in the Supplemental Materials on the ASME Digital Collection). We minimize temperature variations within the microchip by using small dimensions (1 cm × 1 cm × 0.1 cm). Prior to imaging, the microchip is heated to ~75 °C using a hotplate. Fluorescence images are captured every second as the microchip cools down while the solution temperature is recorded every 10 s with a pre-installed thermocouple. The fluorescence intensity increases as the solution temperature decreases as shown in Fig. 2(a). The fluorescence intensities are then normalized by the fluorescence intensity measured at room temperature (25 °C), resulting in a calibration curve (Fig. 2(b)), which is a fourth-order polynomial fit to the data of the form

$$
T = P_0 + P_1 I + P_2 I^2 + P_3 I^3 + P_4 I^4
\tag{9}
$$

where T is the temperature, I is the normalized fluorescence intensity, and P_0–P_4 are fitting constants: $P_0 = (128.7 \pm 2.6)$°C, $P_1 = (-359.5 \pm 20.3)$°C, $P_2 = (589.9 \pm 54.8)$°C, $P_3 = (-499.4 \pm 61.5)$°C, and $P_4 = (165 \pm 24.5)$°C. The fitted line is relatively consistent even at different dye concentrations and matches very well with the past report of Ross et al. [39].

4.1.2 Liquid Thickness Effect on Fluorescence Intensity. To understand the liquid thickness effect on fluorescence intensity, we analyze a liquid meniscus trapped between two glass slides separated by 1 mm. The focal plane is fixed by focusing on a mark created at the bottom of the glass slide, as shown in Fig. 2(c). The meniscus is generated by pipetting 200 μL of rhodamine B solution between the glass slides. We discover an almost linear increase in fluorescence intensity until the liquid thickness reaches ~500 μm (Fig. 2(d)). This is because the light passes through more solution at constant dye concentrations, thereby exciting more fluorophores. However, the fluorescence intensity reaches a plateau when the distance that light can penetrate through the solution is equal to the maximum distance that fluorescence can be sensed (Fig. 2(d)). This relationship between liquid thickness and fluorescence intensity holds for different temperatures (Fig. 2(d)). All the results above infer that varying liquid thickness has substantial influence on fluorescence intensity when the liquid thickness is <500 μm but is less sensitive when liquid thicknesses is >500 μm. Therefore, we minimize the effect of liquid thickness by maintaining a constant liquid thickness through a reservoir in Sec. 4.2.3.

4.1.3 Concentration Effect on Fluorescence Intensity. We quantify how dye concentration impacts fluorescence intensity in an open system environment. To do this, we compare two cases: In one case, we increase the dye concentration by evaporating the dye solution. In the second case, the dye concentration is kept constant while the liquid thickness is adjusted to match the former case. In detail, two 1-cm-diameter wells are filled with 1 mM rhodamine B solution, as shown in the inset of Fig. 2(e). The solution of one well is exposed to air at room temperature to promote evaporation, whereas the other is sealed to prevent it. The liquid thickness and fluorescence intensity are measured for both wells in sequential time-steps where the second well's solution is pulled
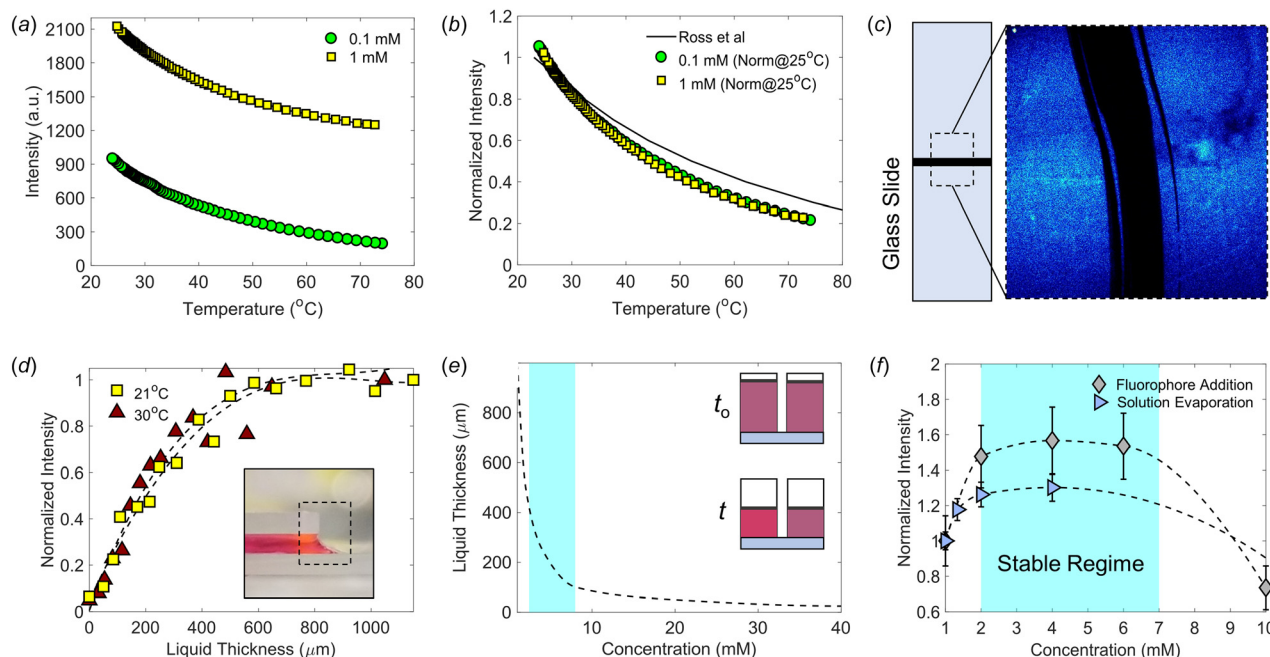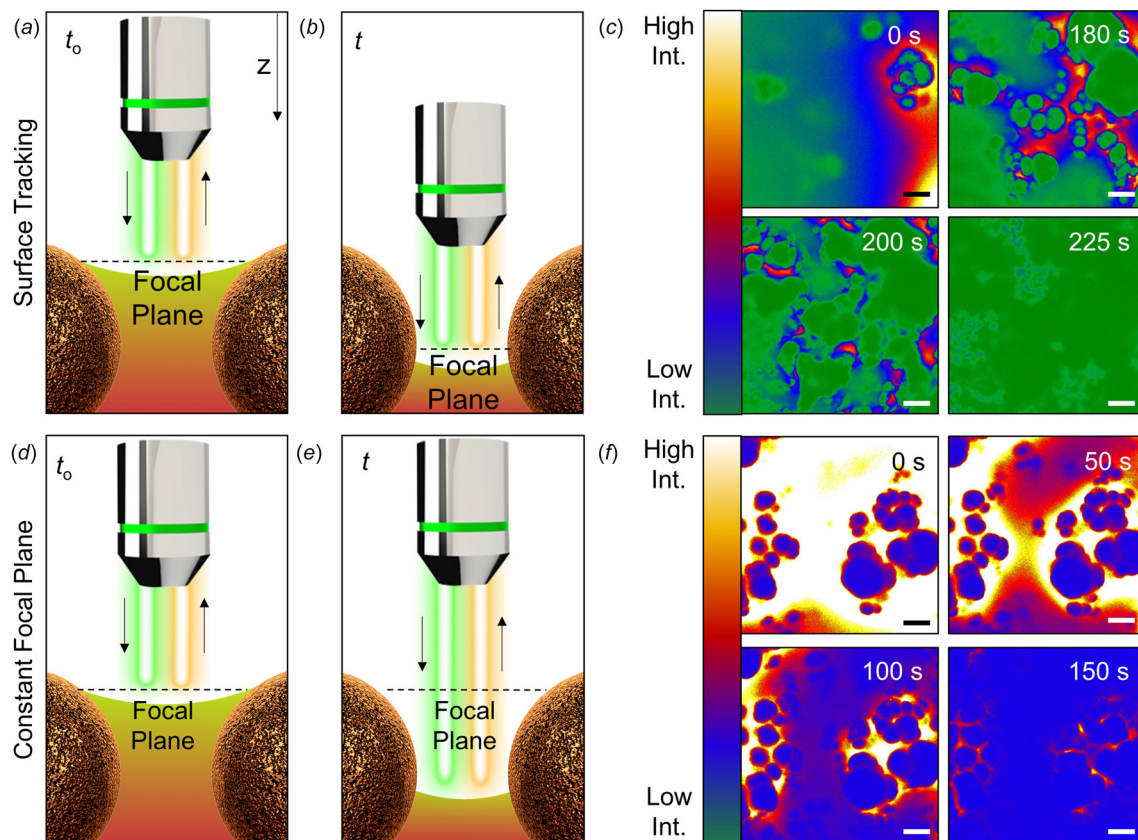
Fig. 2 Characterization of rhodamine B solution. (*a*) The plot shows that the fluorescence intensity of rhodamine B decreases as temperature increases. The decreasing trend is relatively independent of concentration. It should be noted that the gain of the 1 mM concentration case is set to a lower value than the 0.1 mM case due to excessive fluorescence signals. (*b*) The temperature-fluorescence intensity calibration curve is created by normalizing cold-field intensity values at 25 °C. The calibration curve shows excellent consistency between different concentrations and a good match with a previous research by Ross et al. (*c*) The focal length is fixed by maintaining a constant focus on the bottom slide. The focal length is initially determined by focusing on a marker as shown. (*d*) The fluorescence intensity exhibits an almost linear increasing trend with liquid thickness up to ~500 μm. The measured fluorescence intensity values are normalized with intensity peak values for each experiment. Inset shows how a meniscus is formed between two glass slides. The scale bar is 1 mm. (*e*) A concentration estimation curve of an evaporating solution is plotted where the liquid thickness represents the amount of solution left. Insets show liquid thicknesses at different time frames. (*f*) The concentration effect on fluorescence intensity is plotted, showing the existence of a stable regime that is relatively independent of concentration between 2 and 7 mM.

out manually every time-step to match the first well's liquid thickness. Both wells' fluorescence intensity increases as the solution evaporates when the liquid thickness is below 1 mm, which agrees with the previous observation. The estimated evaporation-induced concentration variations with respect to liquid thickness from a known initial fluorophore mass is plotted in Fig. 2(*e*). The fluorescence intensity increases 30% as the concentration increases from 1 mM to 2 mM but reaches a relatively stable regime at concentrations 2–7 mM (Fig. 2(*f*)). This trend is further validated through a separate case where concentration is increased by adding fluorophores at a fixed volume (Fig. 2(*f*)). The 15%–20% error between the two approaches may be attributed to fluorophores escaping the liquid through evaporation or by adhering to the surrounding walls. The drastic fluorescence intensity drop after the stable regime is caused by the self-quenching of fluorophores and has been reported elsewhere [42]. In other words, our results show that ~90% of the experimental process occurs at concentrations between 1 and 10 mM. Therefore, in this study we use 2 mM dye concentration as an effort to minimize the concentration effects on the overall fluorescent intensity.

4.2 Characterization of the Wick's Evaporative Performance. To characterize the wick's evaporative performance, we measure evaporation rates at different scales using fluorescence signal tracking and fluorescence thermometry methods. For the following experiments, the sample is heated up at a constant heat flux of 0.75 Wcm^{-2} with an ITO heater installed at the base of the chip. As the solution evaporates, the liquid thickness decreases and causes a reduction in fluorescence intensity. The background-subtracted fluorescence intensity values are defined as the relative fluorescence intensity in this paper.

4.2.1 Overall Evaporation Rate. We measure the overall evaporation rate by tracking the surface fluorescence signals (i.e., surface tracking method) of an evaporating 10 μL rhodamine B solution droplet pipetted into the wick as illustrated in Figs. 3(*a*) and 3(*b*). As the solution surface approaches depletion, the fluorescence intensity rapidly decreases due to the liquid thickness effects (Fig. 2(*d*)). We define the time that the relative intensity decays to 1% of its original value as the overall dry-out time t_{od}. Figure 3(*c*) exhibits real-time fluorescence imaging of the surface-tracking method, showing gradually growing wick features (i.e., circular shapes) along the *z*-axis. The presence of more solid materials at the base of the substrate causes the perceptional growth of the wick features shown in Fig. 3(*c*). It should be noted that the excitation light's inability to penetrate through the solid materials causes the wick structures to have low fluorescence intensity profiles. Finally, the overall evaporation rate, defined as the ratio of the evaporated mass to t_{od}, is measured as 4.44×10^{-5} kgs^{-1}.

4.2.2 Local Dry-Out. In order to relate the microstructures with local evaporation rates, we observe microscale (2–35 μm) local dry-outs. The following experiments follow the same procedures mentioned above but maintains a consistent focal plane (i.e., static focal plane), as shown in Figs. 3(*d*) and 3(*e*). Figure 3(*f*) shows time-dependent images of decaying fluorescence signals on a constant focal plane. In this set of experiments, the fluorescence intensity decreases as the retreating surface (or increasing focal length) impedes signal transmission. We record temporal fluorescence intensity profiles of different liquid–vapor surface areas (i.e., menisci) characterized by taking the average width (i.e., characteristic length) between solid structures, as shown in Fig. 4(*a*). Analogous to t_{od}, the elapsed time for the relative

Fig. 3 Overall and local evaporation rate characterization. (*a*)–(*c*) In the surface-tracking method, the liquid–vapor interface moves along the *z*-axis as the rhodamine B solution evaporates. The fluorescence signal emitted from the liquid–vapor interface is tracked by changing the focus plane (surface-tracking method). (*a*) and (*b*) The figures illustrate the surface-tracking method where (*a*) is the initial state and (*b*) is an arbitrary state during the process. (*c*) Real-time fluorescence images show the fluorescence intensity decay as the rhodamine B droplet evaporates. The scale bar represents 20 μm. (*d*)–(*f*) Unlike the surface-tracking method, the local evaporation rate is characterized by maintaining focus on a consistent plane (*d*) before and (*e*) during the evaporation process. (*f*) Temporal fluorescence images show that the fluorescence intensity decays as the solvent evaporates. The scale bar is 20 μm.
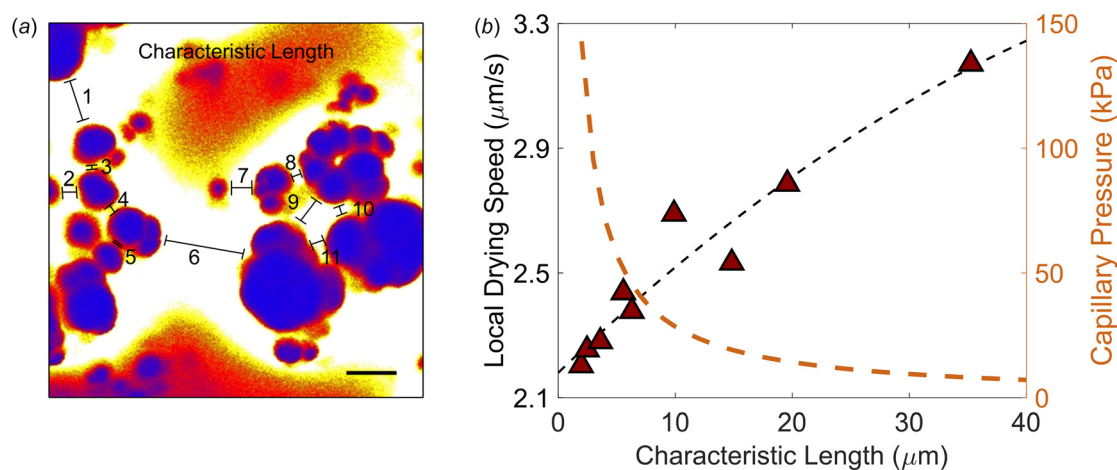
Fig. 4 Microscale dry-out. (*a*) The image shows examples of characteristic lengths of the liquid–vapor surface area between solid particles (circular shapes). The solid particles have low fluorescence intensity profiles which can be attributed to the inability of the excitation light to penetrate through solid materials. The scale bar is 20 μm. (*b*) The local drying speed shows an almost linear increasing trend with longer characteristic length, indicating that the solution dry-out occurs faster for longer characteristic lengths. The capillary pressure estimation plot based on the feature sizes shows that domains with shorter characteristic lengths provide larger capillary forces.
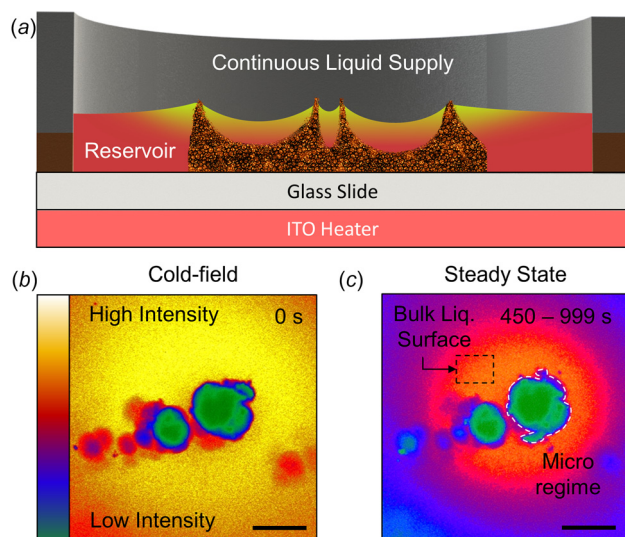
Fig. 5 Local evaporation rate measurement. (*a*) A reservoir continuously supplies liquid to the wick to maintain constant liquid levels during the experiment. Average fluorescence intensities are measured for both the (*b*) cold-field and (*c*) steady-state. The microregime is visually identified by sharp fluorescence intensity-based color contrasts at the peripheral of the solid structure. The bulk liquid surface is approximately 10 μm apart from the solid particle where fluorescence intensity has a relatively uniform profile. The scale bar represents 20 μm.

fluorescence intensity to decrease to 1% of its original value indicates the local dry-out time t_{ld}. In addition, the local drying speed u_{ld}, which is calculated by dividing the average structural height by t_{ld} characterizes microscale dry-out. u_{ld} increases almost linearly with longer characteristic lengths, which implies that liquid sections with larger liquid–vapor interface areas dries faster than sections with smaller ones.

4.2.3 Local Evaporation Rate. We finally investigate submicron level ($\sim0.3\,\mu$m) evaporation rates by utilizing the dye's temperature-sensitive properties. This procedure consists of three steps: (1) measuring surface fluorescence intensity of a heated solution in a steady-state, (2) converting the measured fluorescence intensity to surface temperature, and (3) calculating local evaporation rates based on the obtained surface temperature profiles.

In the following experiment, a 300-μL reservoir maintains a constant liquid thickness within the porous structure upon

evaporation (Fig. 5(*a*)). The initial state (i.e., cold field) (Fig. 5(*b*)) is considered to reach a steady-state (Fig. 5(*c*)) when the fluorescence intensity contours remains noticeably unchanged for at least $400\,$s. Furthermore, the borderline located between the liquid and solid contours (approximately 0.3–$1\,\mu$m from the solid contour) represents the microregime. The fluorescence intensity is then normalized by the cold field bulk liquid surface intensity for the calibration.

The local surface temperature of the bulk liquid surface and microregime is obtained by fitting the normalized fluorescence intensity values into the calibration curve in Eq. (9). The converted average surface temperatures of the bulk liquid surface and the microregime are $34.9\,°$C and $40.9\,°$C, respectively.

As the final step, we calculate the local evaporative mass flux by applying the converted surface temperature values into Eq. (5). The obtained evaporation rates of the bulk liquid and microregime are 0.00074 and $0.0011\,$kgm^{-2}s^{-1}, respectively. The results suggest that highly evaporative areas (i.e., microregimes) form near (~0.3–$1\,\mu$m) the solid–vapor–liquid interfaces.

4.3 Microscopic Liquid Pathways. Our results not only characterize overall and local evaporative phenomena but also explain passive microscopic liquid flow paths occurring within microscale structures. Based on the measured data, the microregime exhibits a $\sim50\%$ increase in evaporative mass flux (Fig. 6(*a*)) when compared to the bulk regime. The high evaporation associated with the microregime (also identified as the thin-film region in some papers) agrees with previous reports where the microregime is found to contribute up to 80% of the overall heat transfer occurring from the entire meniscus [44–47]. A recent study reports higher evaporation rates at liquid–vapor interfaces with smaller characteristic lengths by using computational fluid dynamics models [46]. In other words, liquid domains with smaller menisci have high evaporation rates because a larger portion of the menisci is influenced by the microregime. However, we report shorter local drying speed for smaller characteristic lengths (Fig. 4(*b*)) which may seem counterintuitive to the prior statement. We attribute this to the capillary-driven flow due to the microstructures (Fig. 4(*b*)). The plot provided in Fig. 4(*b*) estimates significant increases in capillary pressure as the characteristic length decreases, leading to enhanced capillary filling between smaller feature sizes. This potentially explains why smaller feature sizes can exhibit longer local drying speeds despite having higher evaporation rates, as illustrated in Fig. 6(*b*).

4.4 Limitations of Estimating Liquid–Vapor Interface Effects. The understanding about liquid–vapor interfaces between submicron features is crucial in collecting accurate surface
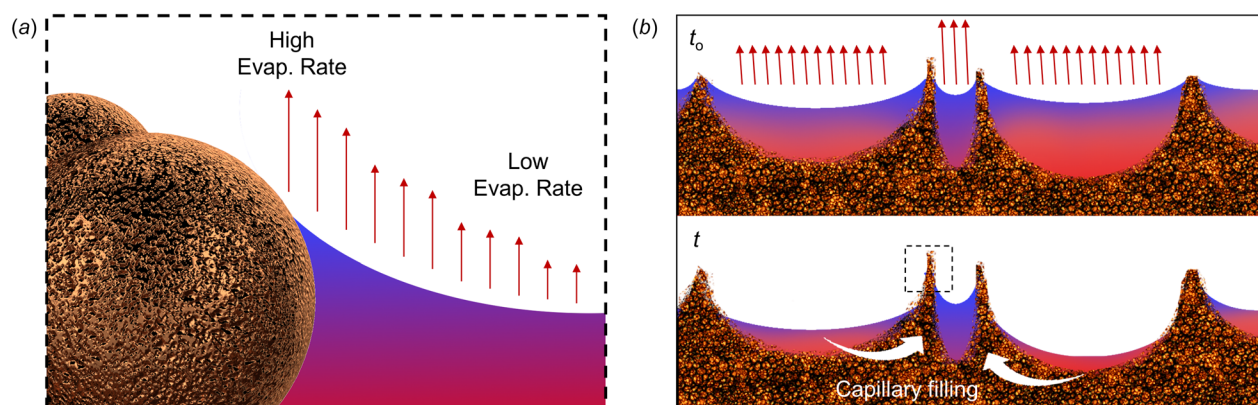
Fig. 6 Evaporation-induced liquid flow paths within microscale structures. (*a*) The local evaporation rate near the liquid–vapor–solid contact line is higher than the local evaporation rate of the bulk liquid. (*b*) The illustrations show capillary filling into microcavities with smaller feature sizes where t_o is the initial state after liquid is wicked and t is an arbitrary state during the evaporation process.

temperature data used to calculate heat transfer performances. The random and tortuous nature of the microstructures used in this study obscures the visualization from the sideview and makes it difficult to reconstruct the meniscus shape experimentally or computationally. Therefore, we assume that the liquid thickness effect on fluorescence intensity explained in Fig. 2(*d*) is mainly governed by the bulk liquid thickness rather than the microscopic liquid thickness variations caused by the liquid–vapor interface between the microstructures. Still, obtaining an accurate liquid–vapor interface model can help clarify where the microregime is located and improve the accuracy of the current measurements. For the current study, we acquire a relatively large temperature difference (~6 °C) between the microregime and the bulk liquid. To minimize those limitations, future work will employ well-controlled microstructures that can help us to estimate the meniscus geometry between microstructures and to classify the micro- and bulk liquid regimes.

5 Conclusion

In this study, we analyze the local and average evaporative performances of microstructures using μLIF techniques at the submicron scales. We show the potential of the use of μLIF techniques for evaporation characterizations by separating the interplaying parameters such as temperature, liquid thickness, and dye concentration of rhodamine B solutions. A series of techniques involving dynamic surface-tracking and static focal plane measurements of fluorescence signals have been demonstrated to characterize overall and local liquid dry-outs. Furthermore, we show that submicron level evaporation rates can be measured by retrieving surface temperature information converted from fluorescence signals. The integrated results infer that liquid confined between small characteristic lengths exhibits higher evaporation rates with slower drying rates. The slower drying rates might be attributed to the continuous liquid supply from the vicinity through capillary feeding. The μLIF techniques introduced in this work will enable researchers to precisely characterize microscale thermofluidic properties in thermal/fluid applications. Further work is needed to understand the microscopic liquid thickness effects on fluorescence intensity through reconstructed meniscus shapes between well-defined microstructures.

Nomenclature

C = vapor molar concentration, mol m^{-3}
D = diffusion coefficient in air, m^2 s^{-1}
h = average structural thickness, μm
h_{fg} = enthalpy of evaporation, J kg^{-1}
I = fluorescence intensity, a.u
L = length, μm
m = mass, kg
M = molecular weight, kg mol^{-1}
$\dot{m}''$ = mass flux, kg m^{-2} s^{-1}
p = pressure, Pa
P = fitting coefficient, K
R = universal gas constant, J mol^{-1} K^{-1}
t = time, s
T = absolute temperature, K
u = fluid velocity, ms^{-1}
v = speed, μ ms^{-1}

Subscripts

air = air
atm = atmospheric pressure
far = $3h$ distance from liquid–vapor interface
ld = local drying
lv = liquid–vapor interface
n = component along $\vec{n}$ direction
od = overall drying
ref = reference
sat = saturated
tot = vapor and air
v = vapor

References

[1] Pop, E., 2010, "Energy Dissipation and Transport in Nanoscale Devices," Nano Res., **3**(3), pp. 147–169.
[2] Faghri, A., 2012, "Review and Advances in Heat Pipe Science and Technology," ASME J. Heat Transfer, **134**(12), p. 123001.
[3] Launay, S., Sartre, V., and Bonjour, J., 2007, "Parametric Analysis of Loop Heat Pipe Operation: A Literature Review," Int. J. Therm. Sci., **46**(7), pp. 621–636.
[4] Yeh, C. C., Chen, C. N., and Chen, Y. M., 2009, "Heat Transfer Analysis of a Loop Heat Pipe With Biporous Wicks," Int. J. Heat Mass Transfer, **52**(19–20), pp. 4426–4434.
[5] Weisenseel, B., Greil, P., and Fey, T., 2017, "Biomorphous Silicon Carbide as Novel Loop Heat Pipe Wicks," Adv. Eng. Mater. **19**(1), p. 1600379.
[6] Huminic, G., Huminic, A., Morjan, I., and Dumitrache, F., 2011, "Experimental Study of the Thermal Performance of Thermosyphon Heat Pipe Using Iron Oxide Nanoparticles," Int. J. Heat Mass Transfer, **54**(1–3), pp. 656–661.
[7] de Bock, H. P. J., Varanasi, K., Chamarthy, P., Deng, T., Kulkarni, A., Rush, B. M., Russ, B. A., Weaver, S. E., and Gerner, F. M., 2009, "Experimental Investigation of Micro/Nano Heat Pipe Wick Structures," IMECE 2008: Heat Transfer, Fluid Flows, and Thermal Systems, Vol. 10, Boston, MA, Oct. 31–Nov. 6, pp. 991–996, ASME Paper No. IMEC2008-67288.
[8] De Bock, H. P. J., 2013, "Design and Experimental Validation of a Micro-Nano Structured Thermal Ground Plane for High-g Environments," Ph.D. dissertation, University of Cincinnati, Cincinnati, OH.
[9] Lee, J., Suh, Y., Dubey, P. P., Barako, M. T., and Won, Y., 2019, "Capillary Wicking in Hierarchically Textured Copper Nanowire Arrays," ACS Appl. Mater. Inter., **11**(1), pp. 1546–1554.
[10] Bodla, K. K., Weibel, J. A., and Garimella, S. V., 2013, "Advances in Fluid and Thermal Transport Property Analysis and Design of Sintered Porous Wick Microstructures," ASME J. Heat Transfer, **135**(6), p. 061202.
[11] Kandlikar, S. G., 2017, "Enhanced Macroconvection Mechanism With Separate Liquid-Vapor Pathways to Improve Pool Boiling Performance," ASME J. Heat Transfer, **139**(5), p. 051501.
[12] Li, T., and Peterson, G. P., 2006, "Evaporation/Boiling in Thin Capillary Wicks (II)—Effects of Volumetric Porosity and Mesh Size," ASME J. Heat Transfer, **128**(12), pp. 1320–1328.
[13] Ranjan, R., Murthy, J. Y., Garimella, S. V., and Vadakkan, U., 2011, "A Numerical Model for Transport in Flat Heat Pipes Considering Wick Microstructure Effects," Int. J. Heat Mass Transfer, **54**(1–3), pp. 153–168.
[14] Girard, F., Antoni, M., and Sefiane, K., 2010, "Infrared Thermography Investigation of an Evaporating Sessile Water Droplet on Heated Substrates," Langmuir, **26**(7), pp. 4576–4580.
[15] Hohmann, C., and Stephan, P., 2002, "Microscale Temperature Measurement at an Evaporating Liquid Meniscus," Exp. Therm. Fluid Sci., **26**(2–4), pp. 157–162.
[16] Buffone, C., and Sefiane, K., 2005, "Temperature Measurement Near the Triple Line During Phase Change Using Thermochromic Liquid Crystal Thermography," Exp. Fluids, **39**(1), pp. 99–110.
[17] Pan, Z. H., Dash, S., Weibel, J. A., and Garimella, S. V., 2013, "Assessment of Water Droplet Evaporation Mechanisms on Hydrophobic and Superhydrophobic Substrates," Langmuir, **29**(51), pp. 15831–15841.
[18] Feng, J., Tian, K. J., Hu, D. H., Wang, S. Q., Li, S. Y., Zeng, Y., Li, Y., and Yang, G. Q., 2011, "A Triarylboron-Based Fluorescent Thermometer: Sensitive Over a Wide Temperature Range," Angew. Chem. Int. Ed., **50**(35), pp. 8072–8076.
[19] Mishan, Y., Mosyak, A., Pogrebnyak, E., and Hetsroni, G., 2007, "Effect of Developing Flow and Thermal Regime on Momentum and Heat Transfer in Micro-Scale Heat Sink," Int. J. Heat Mass. Transfer, **50**(15–16), pp. 3100–3114.

[20] Carlomagno, G. M., and Cardone, G., 2010, "Infrared Thermography for Convective Heat Transfer Measurements," Exp. Fluids, **49**(6), pp. 1187–1218.

[21] Christofferson, J., Maize, K., Ezzahri, Y., Shabani, J., Wang, X., and Shakouri, A., 2007, "Microscale and Nanoscale Thermal Characterization Techniques," International Conference on Thermal Issues in Emerging Technologies—Theory and Applications, Cairo, Egypt, Jan. 3–6, p. 3+.

[22] Dhavaleswarapu, H. K., Garimella, S. V., and Murthy, J. Y., 2009, "Microscale Temperature Measurements Near the Triple Line of an Evaporating Thin Liquid Film," ASME J. Heat Transfer, **131**(6), p. 061501.

[23] Low, P., Kim, B., Takama, N., and Bergaud, C., 2008, "High-Spatial-Resolution Surface-Temperature Mapping Using Fluorescent Thermometry," Small, **4**(7), pp. 908–914.

[24] Kenning, D. B. R., and Yan, Y. Y., 1996, "Pool Boiling Heat Transfer on a Thin Plate: Features Revealed by Liquid Crystal Thermography," Int. J. Heat Mass Transfer, **39**(15), pp. 3117–3137.

[25] Ekkad, S. V., and Han, J. C., 2000, "A Transient Liquid Crystal Thermography Technique for Gas Turbine Heat Transfer Measurements," Meas. Sci. Technol., **11**(7), pp. 957–968.

[26] Brites, C. D. S., Lima, P. P., Silva, N. J. O., Millan, A., Amaral, V. S., Palacio, F., and Carlos, L. D., 2012, "Thermometry at the Nanoscale," Nanoscale, **4**(16), pp. 4799–4829.

[27] Tovee, P. D., and Kolosov, O. V., 2013, "Mapping Nanoscale Thermal Transfer in-Liquid Environment-Immersion Scanning Thermal Microscopy," Nanotechnology, **24**(46), p. 465706.

[28] Assy, A., and Gomes, S., 2015, "Temperature-Dependent Capillary Forces at Nano-Contacts for Estimating the Heat Conduction Through a Water Meniscus," Nanotechnology, **26**(35), p. 355401.

[29] Wilson, A. A., and Sharar, D. J., 2018, "Temperature-Dependent Adhesion Mechanisms of Metal and Insulator Probe-Sample Contact Pairs," Intersociety Conference on Thermal Phenomena in Electronic Systems, San Diego, CA, May 29–June 1, pp. 240–245.

[30] Martinek, J., Klapetek, P., and Campbell, A. C., 2015, "Methods for Topography Artifacts Compensation in Scanning Thermal Microscopy," Ultramicroscopy, **155**, pp. 55–61.

[31] Menges, F., Mensch, P., Schmid, H., Riel, H., Stemmer, A., and Gotsmann, B., 2016, "Temperature Mapping of Operating Nanoscale Devices by Scanning Probe Thermometry," Nat. Commun., **7**(1), pp. 1–6.

[32] Rochlitz, H., and Scholz, P., 2018, "Application of Laser-Induced Fluorescence Technique in a Duct Flow With One Heated Wall," Exp. Fluids, **59**(3), p. 54.

[33] Volkov, R. S., and Strizhak, P. A., 2017, "Planar Laser-Induced Fluorescence Diagnostics of Water Droplets Heating and Evaporation at High-Temperature," Appl. Therm. Eng., **127**, pp. 141–156.

[34] Chaze, W., Caballina, O., Castanet, G., and Lemoine, F., 2017, "Spatially and Temporally Resolved Measurements of the Temperature Inside Droplets Impinging on a Hot Solid Surface," Exp. Fluids, **58**(8), p. 9.

[35] Feng, J., Xiong, L., Wang, S. Q., Li, S. Y., Li, Y., and Yang, G. Q., 2013, "Fluorescent Temperature Sensing Using Triarylboron Compounds and Microcapsules for Detection of a Wide Temperature Range on the Micro- and Macroscale," Adv. Funct. Mater., **23**(3), pp. 340–345.

[36] Erickson, D., Sinton, D., and Li, D. Q., 2003, "Joule Heating and Heat Transfer in Poly(Dimethylsiloxane) Microfluidic Systems," Lab Chip, **3**(3), pp. 141–149.

[37] Samy, R., Glawdel, T., and Ren, C. L., 2008, "Method for Microfluidic Whole-Chip Temperature Measurement Using Thin-Film Poly(Dimethylsiloxane)/Rhodamine B," Anal. Chem., **80**(2), pp. 369–375.

[38] Glawdel, T., Almutairi, Z., Wang, S., and Ren, C., 2009, "Photobleaching Absorbed Rhodamine B to Improve Temperature Measurements in PDMS Microchannels," Lab Chip, **9**(1), pp. 171–174.

[39] Ross, D., Gaitan, M., and Locascio, L. E., 2001, "Temperature Measurement in Microfluidic Systems Using a Temperature-Dependent Fluorescent Dye," Anal. Chem., **73**(17), pp. 4117–4123.

[40] Vetrone, F., Naccache, R., Zamarrón, A., Juarranz de la Fuente, A., Sanz-Rodríguez, F., Martinez Maestro, L., Martín Rodriguez, E., Jaque, D., García Solé, J., and Capobianco, J. A., 2010, "Temperature Sensing Using Fluorescent Nanothermometers," ACS Nano, **4**(6), pp. 3254–3258.

[41] Sakakibara, J., Hishida, K., and Maeda, M., 1993, "Measurements of Thermally Stratified Pipe-Flow Using Image-Processing Techniques," Exp. Fluids, **16**(2), pp. 82–96.

[42] Fikry, M., Omar, M. M., and Ismail, L. Z., 2011, "Effect of Host Medium on the Fluorescence Emission Intensity of Rhodamine B in Liquid and Solid Phase," Modern Trends in Physics Research: Third International Conference on Modern Trends in Physics Research, Cairo, Egypt, Apr. 6–10, pp. 210–219.

[43] Greszik, D., Yang, H., Dreier, T., and Schulz, C., 2011, "Measurement of Water Film Thickness by Laser-Induced Fluorescence and Raman Imaging," Appl. Phys. B-Lasers O, **102**(1), pp. 123–132.

[44] Wang, H., Garimella, S. V., and Murthy, J. Y., 2007, "Characteristics of an Evaporating Thin Film in a Microchannel," Int. J. Heat Mass Transfer, **50**(19–20), pp. 3933–3942.

[45] Bodla, K. K., Murthy, J. Y., and Garimella, S. V., 2013, "Evaporation Analysis in Sintered Wick Microstructures," Int. J. Heat Mass Transfer, **61**, pp. 729–741.

[46] Montazeri, K., Lee, H., and Won, Y., 2018, "Microscopic Analysis of Thin-Film Evaporation on Spherical Pore Surfaces," Int. J. Heat Mass Transfer, **122**, pp. 59–68.

[47] Ranjan, R., Murthy, J. Y., and Garimella, S. V., 2009, "Analysis of the Wicking and Thin-Film Evaporation Characteristics of Microstructures," ASME J. Heat Transfer, **131**(10), p. 101001.